

www.acsaem.org Article

# Isolation of Grain versus Intergranular Transport in $Li_{1+x}Ti_xTa_{1-x}SiO_5$ Suggests Concerted Ion Migration in a High-Voltage Stable Electrolyte from High-Throughput Descriptors

Yu-Ying Lin, Carlos Juarez-Yescas, Kai-Wei Lan, Paul V. Braun, Jessica A. Krogstad,\* and Nicola H. Perry\*



**Cite This:** ACS Appl. Energy Mater. 2023, 6, 11468–11480



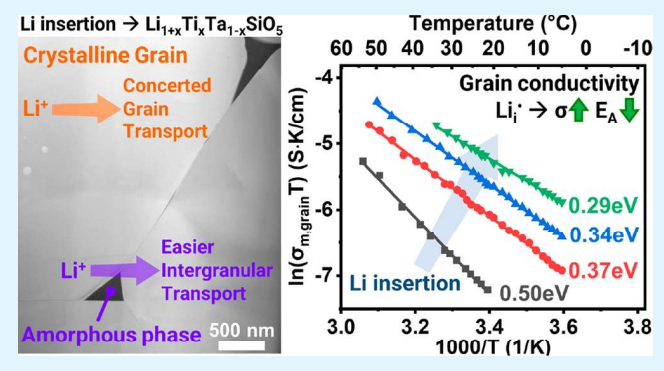
**ACCESS** I

Metrics & More

Article Recommendations

s Supporting Information

**ABSTRACT:** LiTaSiO<sub>5</sub>, with its suitable conduction channels and wide electrochemical stability window, has been previously suggested as a potential host of concerted Li migration triggered by inserting Li interstitials. However, without proper separation of grain and grain boundary contributions, previous experimental efforts have been unable to isolate and quantitatively characterize the defect chemistry—conductivity relationship within the lattice. In this work, LiTaSiO<sub>5</sub> was identified by descriptor filtering of the Materials Project database, and Li<sub>1</sub>• were inserted via Ti<sub>Ta</sub>′ doping to form Li<sub>1+x</sub>Ti<sub>x</sub>Ta<sub>1-x</sub>SiO<sub>5</sub>. The grain and intergranular conductivities were separated using electrochemical impedance spectroscopy with distribution of relaxation times analysis (EIS/DRT). We showed the first clear observation of a monotonic



decrease in activation energy  $E_A$  from 0.50 to 0.29 eV and a 6× increase in Li<sup>+</sup> conductivity in the grains to 2.49 × 10<sup>-5</sup> S/cm for x = 0.15 (30 °C) as more Li<sub>i</sub><sup>•</sup> were inserted, providing insight into how Li<sub>i</sub><sup>•</sup> potentially triggered concerted transport. The necessity of separating grain and grain boundary contributions was further emphasized by observation, via STEM-EDS, of a Si-rich/Ta-poor intergranular amorphous phase that increases in volume with increasing Ti<sub>Ta</sub>′ concentration. This phase led to a 19× increased specific grain boundary conductivity to 5.95 × 10<sup>-6</sup> S/cm for x = 0.15 (30 °C) with decreased  $E_A$ . The distribution of the intergranular phase was inhomogeneous (variation in size, stoichiometry), resulting in a wide distribution of relaxation times for the intergranular transport. Li<sub>1+x</sub>Ti<sub>x</sub>Ta<sub>1-x</sub>SiO<sub>5</sub> also exhibited wide electrochemical stability, up to 4.9 V, making it suitable for application as a solid electrolyte or cathode coating.

**KEYWORDS:** grain conductivity, concerted ion transport, specific grain boundary conductivity, intergranular phase, electrochemical stability

## 1. INTRODUCTION

Li-ion batteries are developing rapidly to support various applications, from mobile devices to electric vehicles and gridlevel storage. With an ever-increasing need for better performance, all-solid-state batteries (ASSB) have drawn significant attention because of their potential to offer higher energy density and better safety. To realize ASSB, the development of new solid electrolyte materials to replace liquid electrolytes is of vital importance. For that reason, researchers have developed and studied many promising Li+ conductors. However, issues like poor interface stability/compatibility, limited electrochemical stability window, poor air stability, and high mechanical stiffness still present as hurdles toward their application in full cells. <sup>1,2</sup> In addition to concentrated efforts to break through the aforementioned limitations by engineering existing materials, the discovery and exploration of new solid electrolyte compositions is another important route to realize ASSB.<sup>3</sup>

In this work, we rediscovered (via high-throughput screening) and explored (electrically, electrochemically, chemically, and structurally) an emerging class of Li<sup>+</sup> conductors, based on LiTaSiO<sub>5</sub>. Previous work by Xiong et al.<sup>9</sup> and Wang et al.<sup>10</sup> suggested computationally that the insertion of Li interstitials into this composition could trigger concerted ion transport—a desirable mechanism for superionic Li conductivity with low effective migration barriers.<sup>11–19</sup> In addition to increasing carrier concentration, the extra Li<sup>+</sup> inserted through acceptor doping in Li<sub>1+x</sub>Zr<sub>x</sub>Ta<sub>1-x</sub>SiO<sub>5</sub> was reported to displace some Li<sup>+</sup>

Received: July 3, 2023
Revised: October 22, 2023
Accepted: October 25, 2023
Published: November 13, 2023





originally on the low-energy site (Li1) to occupy the high-energy site (Li10). 9,10 As a result, the Li<sup>+</sup> sublattice became more disordered, and mobile ions migrating downhill from highenergy sites balanced out a part of the energy barrier encountered by other uphill-climbing ions. These strong interactions between mobile ions can effectively reduce the migration energy barriers and increase the ionic conductivity. This concerted mechanism has also been reported to be responsible for high ionic conductivity in many superionic conductors (SIC), 19 assuming a long-range ordered crystalline lattice without extended defects. However, in practical use, SICs are typically polycrystalline or not fully crystalline, and performance is commonly measured in the form of total conductivity, which consists of the contributions from both grain and intergranular/grain boundary (GB) transport. In previous experimental work on Li<sub>1+x</sub>Zr<sub>x</sub>Ta<sub>1-x</sub>SiO<sub>5</sub>, grain and GB transport were not deconvolved, <sup>9,10</sup> and monotonic trends in activation energy with doping were not observed. Without evaluating the two processes separately and without observing a monotonic trend, the effect of Li<sup>+</sup> insertion on concerted ion transport within the grains remains unconfirmed, even if the total conductivity increased and activation energy decreased. This separation is particularly important for solid electrolytes containing glass-forming elements, like Si in the present case, as there is a reasonable expectation of amorphous regions, such as intergranular phases, that also contribute to the measured total conductivity. Therefore, in our work we focused on this necessary isolation of grain and grain boundary/intergranular contributions to transport through careful microstructure, ac impedance, and relaxation time analysis.

Using a descriptor-based screening approach of nearly 16000 Li-containing compositions in the Materials Project (MP) database, LiTaSiO5 was identified as a promising material with desirable properties for solid electrolytes (i.e., low electronic conductivity, suitable conduction channels, and an electrochemical stability window suitable for use with high-voltage cathodes). Into this composition we experimentally substituted a portion of Ta<sup>5+</sup> with Ti<sup>4+</sup> acceptors to introduce systematically varied amounts of Li interstitials for charge compensation, making the final compositions  $\text{Li}_{1+x}\text{Ti}_x\text{Ta}_{1-x}\text{SiO}_5$  (x = 0, 0.05,0.1, 0.15). Ti<sup>4+</sup> (0.605 Å) has a similar ionic radius to Ta<sup>5+</sup> (0.64 Å), which could potentially lead to better dopability compared to the previously explored dopant Zr4+ (0.72 Å) and potentially minimize chemo-mechanical effects on transport. We explored the synthesis parameters for  $Li_{1+x}Ti_xTa_{1-x}SiO_5$ , followed by indepth microstructure and transport studies. Li<sub>1+x</sub>Ti<sub>x</sub>Ta<sub>1-x</sub>SiO<sub>5</sub> consisted of mostly crystalline grains with an intergranular amorphous phase. We carefully separated the grain and grain boundary transport processes to (1) more clearly understand the effect of Li<sup>+</sup> insertion within the crystalline lattice and (2) correlate the intergranular/GB transport behavior with the microstructure and local composition. Furthermore, in the screening process, additional electrolyte candidates were identified that are expected to exhibit favorable ionic conductivity behavior with either high or low voltage stability.

# 2. METHODS

**2.1. Screening for Solid Li**<sup>+</sup> **Conductors.** Before the in-depth experimental efforts, our initial selection of LiTaSiO<sub>5</sub> arose from a high-throughput descriptor filtering process to identify candidate compositions with desirable properties as solid electrolyte material. In the screening process, materials properties such as bandgap and energy above the convex hull were directly obtained from MP using pymatgen

packages.<sup>20</sup> For example, the bandgap is related to intrinsic electronic conductivity, and energy above the hull is associated with thermodynamic stability. The thermodynamic electrochemical stability window was also obtained from MP using the pymatgen.analysis.phase diagram module. By variation of the chemical potential of Li, it determines the range in which a certain composition can be thermodynamically stable. Additional calculations were performed to evaluate the migration energy. Bond valence migration energy  $(E_{\rm m,BV})^{21,22}$  evaluates the electrostatic interactions between Li<sup>+</sup> and other immobile framework ions and was used to ensure that the framework scaffolds form conduction channels and allow for Li<sup>+</sup> conduction. Although there are some inherent limits in  $E_{\rm m,BV}$ calculations, it is one of the fastest routes to estimate the ability for Li<sup>+</sup> transport (1–2 min/structure on a personal computer);  $E_{mBV}$  has also been shown to positively correlate with activation energies  $(E_A)$ calculated by DFT.<sup>23</sup> By first assigning the oxidation states of the ions with the program FormalCharges, <sup>24</sup> the bond valence migration energy  $(E_{\rm m,BV})$  was calculated using the program BondStr.<sup>2</sup>

These calculations were performed for many Li-containing compounds in MP, similar to our previous work, where we used a slightly different descriptor filter.<sup>26</sup> After obtaining important properties for electrolytes, the compositions were filtered, with the filtering steps/selection criteria illustrated in Figure 1 and outlined here: (1) All

	Ternary	Quaternary
(1) All Li compounds (Materials Project)	5264	11545
(2) Bandgap ≥ 1 eV	1766	5906
Energy above hull ≤ 50 meV	1018	3016
(4) Exclude transition metal (V. Cr. Mn. Fe. Co. Ni, Cu)	589	1179
(5) Bond Valence E <sub>A</sub> ≤ 1 eV	236	412
(6) Electrochemical Stability (Left: $V_{red} < 0.5V$ , Right: $V_{ox} > 3.5V$ )	40 49	16 155

Figure 1. Workflow of the filtering process: material properties suitable for solid electrolyte materials were used to downselect compositions. Steps 1–5 ensured low electronic conductivity, low energy above the hull, and low migration energy. For ternary and quaternary compounds, in step 6, the left split arrows selected compositions with stability against low-voltage anodes, and the right split arrows selected materials with stability against high-voltage cathodes; LiTaSiO $_{\rm S}$  was one of the candidates in this category ( $V_{\rm red}$  and  $V_{\rm ox}$  are respectively the calculated thermodynamic reduction and oxidation stabilities vs Li).

Li-containing compounds were taken from MP and categorized into ternary and quaternary compounds (binary compounds and others were excluded). At the time of the search, there were 5264 ternary and 11545 quaternary Li-containing compounds. (2) A large bandgap is preferable for solid electrolyte materials to limit intrinsic electronic conductivity. Bandgaps from MP are often underestimated as they are calculated by DFT using the generalized gradient approximation (GGA) functional. Therefore, a relatively low cutoff value of >1 eV was chosen as a starting point. (3) To ensure their thermodynamic stability, only compounds with energy above hull ≤50 meV/atom were allowed to pass. 50 meV/atom was used as a rule of thumb for phase stability because of prediction errors of DFT calculations using the GGA functional. (4) Compounds containing potentially multivalent transition metals (V, Cr, Mn, Fe, Co, Ni, Cu) were excluded to limit the probability of electronic conductivity and redox activity. (5) Only

compounds with a  $E_{\rm m,BV} \leq 1$  eV were chosen to rule out compounds with unsuitable framework-ion sublattices for  ${\rm Li}^+$  transport.  $E_{\rm m,BV}$  tends to overestimate the actual activation energy, with a scaling factor of 0.3–0.7 compared to  $E_{\rm A}$  calculated by DFT. <sup>23,24</sup> With many superionic conductors having an  $E_{\rm A}$  of 0.2–0.5 eV, <sup>1,11,19</sup> we think an intermediate criterion of  $E_{\rm m,BV} \leq 1$  eV correlating to an  $E_{\rm A}$  below 0.3–0.7 eV was reasonable. (6) Compounds with electrochemical stability  $\leq 0.5$  V were selected in the left split arrows for ternary and quaternary compounds—these materials have better compatibility with low-voltage anodes. On the other hand, compounds with electrochemical stability  $\geq 3.5$  V were selected in the right split arrows for ternary and quaternary compounds—these materials have better compatibility with high-voltage cathodes. Experimental electrochemical stability windows tend to be wider than calculated thermodynamic electrochemical stability windows. <sup>19,28</sup> Therefore, intermediate cutoff values of 0.5 or 3.5 V were chosen as starting points.

Additional explanations of the filtering steps can be found in Section 1 of the Supporting Information. The compounds selected in each step are listed in the Excel files in the Supporting Information along with all the material properties calculated (3\_Ternary\_data.xlsx and 4\_Quarternary\_data.xlsx).

**2.2. Synthesis.** LiTi<sub>x</sub>Ta<sub>1-x</sub>SiO<sub>5</sub> (x = 0, 0.05, 0.1, 0.15) pellets were synthesized using solid-state reactions. Chemicals used include Li<sub>2</sub>CO<sub>3</sub> (lithium carbonate, Thermo Scientific, 99.998%), TiO<sub>2</sub> (titanium oxide, Alfa Aesar, 99.99%), Ta<sub>2</sub>O<sub>5</sub> (tantalum oxide, Fisher Scientific, 99.99%), and SiO<sub>2</sub> (silicon oxide, Sigma-Aldrich, 99.5%). Prior to the mixing of the precursors, the SiO<sub>2</sub> powders were annealed at 1300 °C for 24 h, resulting in crystalline SiO<sub>2</sub> powders (confirmed using X-ray diffraction). Water contents of the reagents were measured by separate mass-loss analysis, in which the precursors were dried to anhydrous states at high temperatures and quenched. Then, Li<sub>2</sub>CO<sub>3</sub> (with 10% excess in Li to compensate for Li loss), TiO2, Ta2O5, and SiO2 powders were mixed stoichiometrically and high-energy ball-milled for 1 h in ethanol with zirconia balls to reduce the particle size and facilitate reactions. After ball-milling, the powders were calcined at 700 °C for 3 h. The calcined mixtures were then dry-pressed uniaxially under 125 MPa with a hydraulic press (Carver, Model 4350), followed by sintering to form  $\text{Li}_{1+x}\text{Ti}_x\text{Ta}_{1-x}\text{SiO}_5$  pellets. Undoped pellets (x = 0) were sintered at 1250 °C for 24 h; doped pellets (x = 0.05, 0.1, 0.15) were sintered at 1150 °C for 24 h. All sintering processes were performed in air under the cover of mother powders to reduce Li loss and contamination from the crucibles. Overall sample composition (including Li content) was confirmed to match the nominal targeted composition of selected samples using inductively coupled plasma optical emission spectroscopy (ICP-OES)—first, the samples were transferred into HF/HNO<sub>3</sub>/HCl mixture solutions and digested in a CEM MARS6 microwave digestion system; then, the sample solutions were diluted and analyzed on a PerkinElmer Optima 8300 ICP-OES instrument (the digestion and ICP analyses were performed by the microanalysis laboratory at the University of Illinois Urbana-Champaign).

**2.3. Characterization.** Sample densities were determined from measured masses and geometries of the pellets and expressed in terms of their respective theoretical densities (measured density/theoretical density = %TD, where the theoretical density was obtained from the structure of the crystalline phase). The phase contents of the LiTi<sub>x</sub>Ta<sub>1-x</sub>SiO<sub>5</sub> pellets were examined by X-ray diffraction (XRD) (Bruker D8 Advance XRD; Cu K $\alpha$  radiation; step size: 0.01°; time per step: 0.1 s; panoramic Soller slit). Rietveld refinements of all XRD data were performed using TOPAS with Powder Diffraction Files (PDF) from the International Centre for Diffraction Data (ICDD) database<sup>29</sup> for phase quantification and lattice parameter refinement.  $R_{wp}$  values from Rietveld refinements can be found in Table S1.

The microstructure and grain size of the pellets were characterized by scanning electron microscopy (SEM) (JEOL 7000F Analytical SEM), bright-field transmission electron microscopy (TEM), and scanning transmission electron microscopy (STEM) using high-angle annular dark field (HAADF) detectors (JEOL 2010 LaB $_{\!6}$  TEM and Talos F200X G2 (S) TEM). Energy-dispersive spectroscopy (EDS) analysis was also performed in STEM mode. TEM specimens were prepared

using focused beam (FIB) milling to lift out site-specific lamellae containing several grains and the intergranular phase (Thermo Scios2 dual-beam SEM/FIB).

For electrical measurements, electrodes were deposited by sputtering Au on both faces of the samples and Pt wires were attached as current collectors. Before electrical measurements, the samples were dried in dry air at 400 °C for 8 h to remove any potential contribution from possible proton conductivity. Two-point AC electrochemical impedance spectroscopy (EIS) measurements (Ametek/Solartron ModulabXM ECS impedance analyzer with femtoammeter and potentiostat attachments) were performed in dry Ar/O<sub>2</sub> mixtures (UHP grade,  $p_{O_2}$  = 0.21 atm, flow rate of ~100 sccm) from 20-100 °C in a tube furnace; for measurements at 5–20  $^{\circ}\text{C}\text{,}$  samples were sealed in small airtight plastic box filled with Ar and immersed in a water bath cooling system during EIS. All EIS measurements were performed over a frequency range of 1 MHz to 100 mHz. The impedance spectra were analyzed by equivalent circuit fitting in the frequency range of the sample responses (omitting electrode response), where Boukamp notation (R, resistance; Q, constant phase element) was used to describe the circuits. An equivalent circuit of (RQ)(RQ) was used to fit all of the EIS spectra using ZView. Geometric corrections according to the dimensions of the pellets were applied to calculate measured conductivities ( $\sigma_{\rm m}$ ) from the measured resistances. Selected impedance spectra were also analyzed with a "Distribution of Relaxation Times" (DRT) approach using DRTtools software <sup>30</sup> (methods of discretization: Gaussian; regularization parameter:  $1 \times 10^{-7}$ ; regularization derivative: second-order). Unless otherwise specified, the electrical grain boundary widths and specific grain boundary conductivity were estimated using the brick layer model using eqs 1 and 2

$$d_{\rm GB} = D_{\rm G} \frac{C_{\rm grain} \varepsilon_{\rm grain}}{C_{\rm GB} \varepsilon_{\rm GB}} \tag{1}$$

$$\sigma_{\rm m,GB,spec} = \sigma_{\rm m,GB,eff} \frac{d_{\rm GB}}{D_{\rm G}} \tag{2}$$

where  $d_{\text{GB}}$ ,  $D_{\text{G}}$ ,  $C_{\text{grain}}$ ,  $C_{\text{GB}}$ ,  $\varepsilon_{\text{grain}}$ ,  $\varepsilon_{\text{GB}}$ ,  $\sigma_{\text{m,GB,spec}}$  and  $\sigma_{\text{m,GB,eff}}$  are respectively the electrical grain boundary width, average grain size, grain capacitance, grain boundary capacitance, grain relative permittivity, grain boundary relative permittivity, specific grain boundary conductivity, and effective grain boundary conductivity. For simplicity,  $\sigma_{\text{m,GB,eff}}$  and  $\sigma_{\text{m,GB,spec}}$  are used to represent the conductivity of the intergranular regions (potential contributions from both the intergranular phase and GB). In Figures S11 and S12, we also provide specific grain boundary conductivities calculated using the mean size of the intergranular pockets as electrical grain boundary thickness.

DC polarization experiments were performed using sputtered Au electrodes (which are blocking to Li but nonblocking to electronic carriers and O) at a constant applied voltage of 0.1 V at room temperature, with monitoring of the current as a function of time. To determine the electrochemical stability window, cyclic voltammetry (CV) was performed at room temperature on  $\text{Li}_{1+x}\text{Ti}_x\text{Ta}_{1-x}\text{SiO}_5$  pellets under Ar with the following configuration: Ti current collector sputtered Aulsintered LiTi<sub>x</sub>Ta<sub>1-x</sub>SiO<sub>5</sub> pelletlLi<sub>6</sub>PS<sub>5</sub>Cl powderslLilCul Ti current collector. A buffer layer of Li<sub>6</sub>PS<sub>5</sub>Cl (NEI Corporation) between the Li<sub>1+x</sub>Ti<sub>x</sub>Ta<sub>1-x</sub>SiO<sub>5</sub> pellet and lithium was used to prevent side reactions with Li. Li<sub>6</sub>PS<sub>5</sub>Cl was pelletized to 300 MPa and interfaced with Li at 20 MPa. The Li<sub>1+x</sub>Ti<sub>x</sub>Ta<sub>1-x</sub>SiO<sub>5</sub> was then interfaced with  $\text{Li}_6\text{PS}_5\text{Cl}$  at 20 MPa; the other side of  $\text{Li}_{1+x}\text{Ti}_x\text{Ta}_{1-x}\text{SiO}_5$ was sputtered with Au beforehand for better electrical contact with the Ti current collector. The setup was tested at a constant pressure of 20 MPa to ensure contact, while the potential was swept from 2 to 6 V (0.1 mV/s) with respect to Li as the reference electrode.

## 3. RESULTS

**3.1. Descriptor Filter Outcome.** The details of the automated descriptor filtering calculations are described in Section 2.1, and the outcomes in terms of compositions that satisfied the criteria are provided as Excel files available in the

Supporting Information. As these selection criteria are commonly recognized as desirable properties for solid electrolyte materials, these candidates (provided in the Supporting Information) could be of interest for the future exploration of new electrolyte materials. Additionally, as the MP database grows, more candidates may become available. LiTaSiO<sub>5</sub> was selected among compositions that successfully passed through the filter shown in Figure 1 with oxidation stability >3.5 V, and its calculated properties are listed in Table 1. These properties

Table 1. Calculated Material Properties of LiTaSiO<sub>5</sub>, Exhibiting Large Bandgap from Materials Project (MP), Low  $E_{\rm m,BV}$ , and Good Stability against High Voltage, Make It a Suitable Candidate for Application as a Solid Electrolyte<sup>a</sup>

composition	MP bandgap	$E_{\rm m,BV} \ ({\rm eV})$	$V_{ m red} \left( { m V}  ight) \ \left( { m vs \ Li}  ight)$	$V_{ m ox}\left({ m V} ight) \ \left({ m vs~Li} ight)$
THE CO	(eV)	` ′	` ,	` ′
LiTaSiO,	3.807	0.51	1.406	4.106

 $<sup>^</sup>aE_{\rm m,BV}$  represents the bond valence migration energy;  $V_{\rm red}$  and  $V_{\rm ox}$  are respectively the calculated thermodynamic reduction and oxidation stabilities vs Li.

suggest suitability as a solid electrolyte, and the oxidative stability, in particular, may enable compatibility of LiTaSiO<sub>S</sub> with high-voltage cathodes. However, the total conductivity of undoped LiTaSiO<sub>S</sub> was  $8.39\times 10^{-7}$  S/cm at 30 °C according to our measurements, which was not high enough for application in a solid-state battery. As a result, strategies to improve its conductivity were explored, as will be discussed in the following sections. In addition, experimental methods were used to verify the computationally predicted wide electrochemical window.

3.2. Crystal Structure, Microstructure, and Intergranular Chemistry of  $Li_{1+x}Ti_xTa_{1-x}SiO_5$ . Previous studies have suggested that the introduction of Li, through acceptor doping on the Ta sites may trigger concerted ion transport to improve ionic conductivities. 9,10 In addition, doping also seemed to lead to better sinterability and higher density. 10 In this work, to introduce Li, , Ti<sup>4+</sup> (0.605 Å) was chosen as the dopant on the Ta<sup>5+</sup> (0.64 Å) sites because of its similar ionic radius for potentially better dopability vs the larger Zr<sup>4+</sup> (0.72 Å) dopant previously studied<sup>9, 10</sup> and to potentially avoid large lattice expansion/contraction upon doping that might also impact transport behavior. The monoclinic LiTaSiO<sub>5</sub> structure, with space group P121/c1 (e.g., PDF#: 00-045-0644), remained the dominant crystalline phase in all Li<sub>1+x</sub>Ti<sub>x</sub>Ta<sub>1-x</sub>SiO<sub>5</sub> samples explored in this work (x = 0-0.15), as evident from the XRD data presented in Figure 2. Regardless of dopant concentration, all samples showed <2 wt % of a LiTaO3 impurity phase after sintering, as seen in Table S1. Similar results have been reported previously<sup>9,10</sup>—formation of a small amount of LiTaO<sub>3</sub> seemed inevitable during bulk synthesis of LiTaSiO<sub>5</sub>. Nevertheless, its impact on electrical properties was deemed negligible on the basis of the low conductivity  $(2.35 \times 10^{-15} \text{ S/cm}^{10})$  and limited volume fraction of the LiTaO3 impurity phase. It was also noted that the cell volume decreased going from x = 0 to x = 0.1 and then increased slightly from x = 0.1 to x = 0.15. In all cases, doping with Ti<sup>4+</sup> led to a slight shrinkage in the lattice relative to the undoped composition, likely due to the smaller radius of Ti<sup>4+</sup> compared to Ta<sup>5+</sup>.

The microstructures of sintered  $\text{Li}_{1+x}\text{Ti}_x\text{Ta}_{1-x}\text{SiO}_5$  pellets can be seen in the SEM images in Figure 3, which consist primarily of relatively large (>1  $\mu$ m) crystalline grains, along with an intergranular phase that becomes more evident with increasing

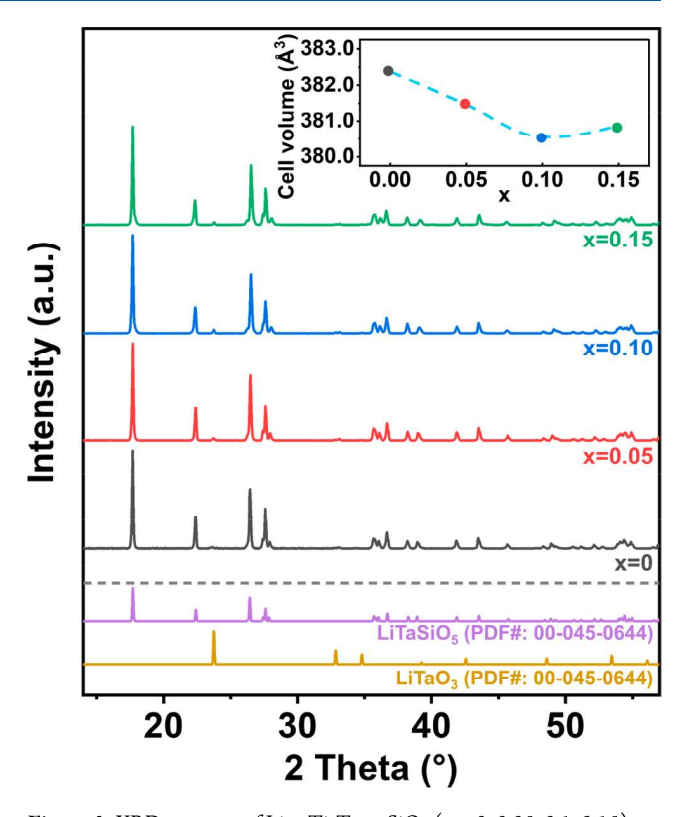


**Figure 2.** XRD patterns of  $\mathrm{Li}_{1+x}\mathrm{Ti}_x\mathrm{Ta}_{1-x}\mathrm{SiO}_5$  (x=0,0.05,0.1,0.15) are plotted above the broken line; reference patterns for phase analysis are shown below the broken line. Undoped pellets (x=0) were sintered at 1250 °C for 24 h; doped pellets (x=0.05,0.1,0.15) were sintered at 1150 °C for 24 h. <2 wt % of  $\mathrm{LiTaO}_3$  impurity phase is observed for all samples. The inset shows the fitted cell volume at different dopant concentrations (the colors of the data points in the inset correspond to the XRD patterns); Ti substitution led to a slightly smaller cell volume compared with the undoped composition.

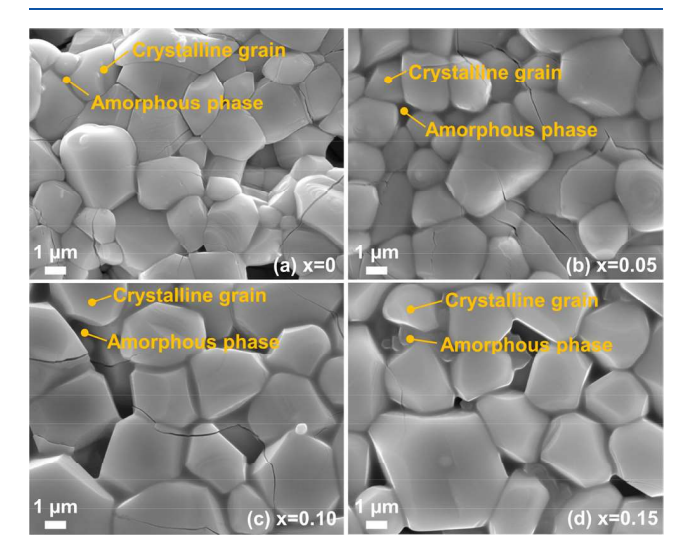


Figure 3. SEM images of  $\text{Li}_{1+x}\text{Ti}_x\text{Ta}_{1-x}\text{SiO}_5$  (x=0,0.05,0.1,0.15). Undoped pellets (x=0) were sintered at 1250 °C for 24 h; doped pellets (x=0.05,0.1,0.15) were sintered at 1150 °C for 24 h. The microstructure consists of mostly crystalline grains with an amorphous phase between grains and along some grain boundaries. As Ti concentration increases, more of the amorphous phase can be observed (also see Figure 4b), along with an increase in grain size (Table S1).

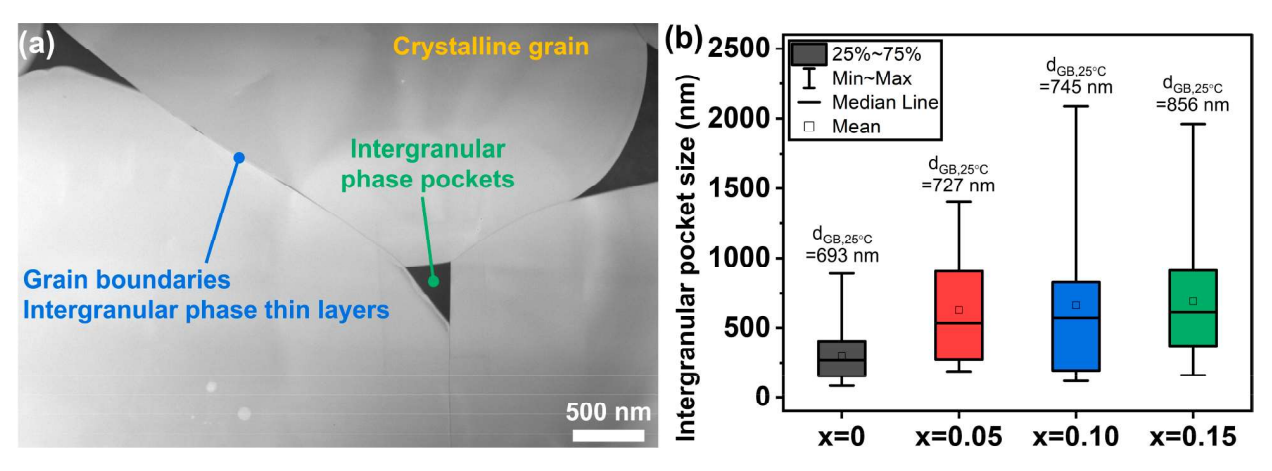


Figure 4. (a) STEM-HADDF image of  $Li_{1.1}Ti_{0.1}Ta_{0.9}SiO_5$  (x = 0.1) sintered at 1150 °C for 24 h, showing intergranular phase pockets between crystalline grains. Thin, Si-rich layers can be found along some GBs, while other GBs ("clean" GB) do not exhibit any chemistry variation with respect to the grain. Samples with different dopant concentrations showed similar microstructural features. Additional high-magnification STEM images and EDS analyses are shown in Figures 5 and 6. (b) Size distribution of the intergranular amorphous pockets as a function of dopant concentration in  $Li_{1+x}Ti_xTa_{1-x}SiO_5$  based on (S)TEM samples; the average sizes were respectively 297, 627, 660, and 714 nm for x = 0, 0.05, 0.10, and 0.15. Larger intergranular amorphous pockets formed as the dopant concentration increased. The sizes of the amorphous pockets and the electrical GB widths ( $d_{GB,25^{\circ}C}$ ) evaluated using the brick layer model (eq 1 with the assumption that the grain and grain boundary relative permittivities are equal) were of the same order.

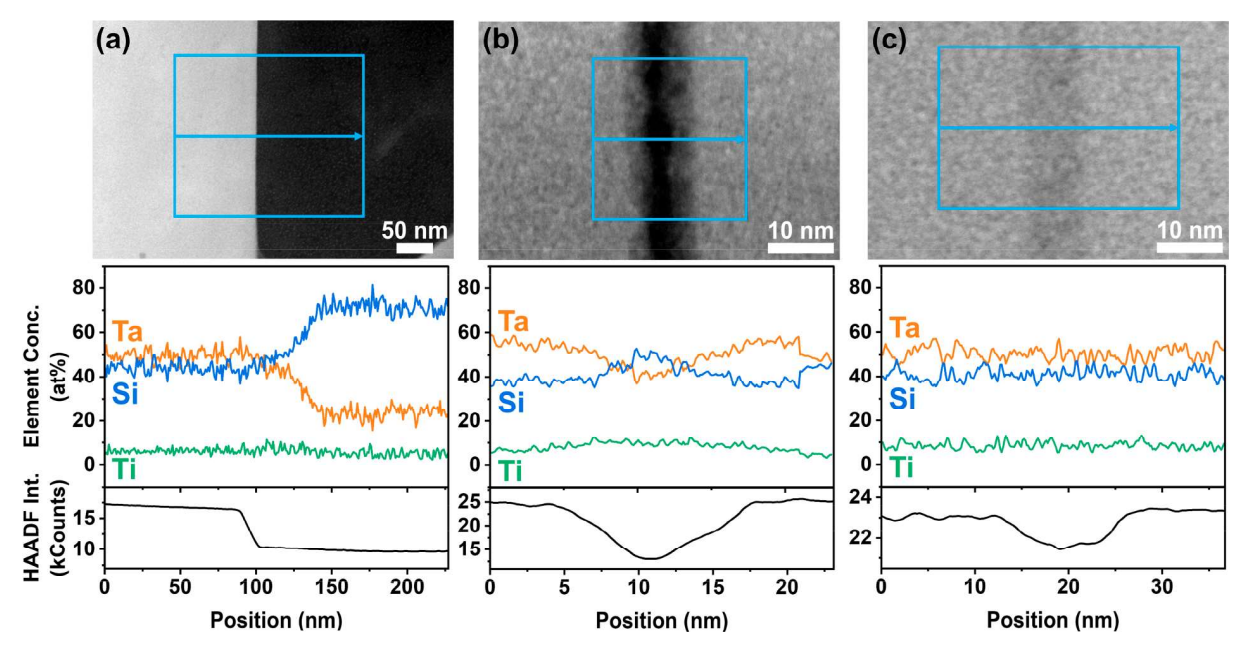


Figure 5. STEM-EDS analysis of different regions in  $\text{Li}_{1.05}\text{Ti}_{0.05}\text{Ta}_{0.95}\text{SiO}_5$  (x=0.05) °C sintered at 1150 °C for 24 h. The EDS and HAADF intensity signals at each position on the arrow were integrated along the direction perpendicular to the arrow, and the blue box shows the bounds of the region in which the signals were integrated. The elemental distribution and HAADF intensity along the light blue arrow are plotted below each micrograph. The crystalline grains have brighter contrast; the intergranular amorphous phase has darker contrast. (a) A pocket of intergranular amorphous phase between grains with significant Si excess. (b) A thin layer of intergranular amorphous phase between two grains with significant Si excess. (c) A "clean" GB showing an unchanging elemental distribution across it and brighter HAADF contrast compared to those of (a) and (b).

Ti concentration. Although less significant, the formation of an intergranular phase was still visible in the microstructure for x=0. Both higher sintering temperatures and higher dopant concentrations led to an increased volume fraction of the intergranular phase. As a result, a lower sintering temperature of  $1150\,^{\circ}\mathrm{C}$  was used for Ti-containing samples, as opposed to  $1250\,^{\circ}\mathrm{C}$  for the undoped samples, to minimize the formation of the amorphous phase. Longer sintering times or slower cooling rates resulted in more impurity phase and amorphous phase formation.

In addition to observation through SEM, the crystalline phase and intergranular phase were examined more closely by (S)TEM. Electron diffraction in TEM confirmed that the grains were crystalline, and the intergranular phase was amorphous (Figure S1). Because of its relatively small volume fraction and amorphous nature, the intergranular phase was not detected by XRD. In STEM-HAADF images (Figures 4–6), crystalline grains had brighter contrast, and the intergranular amorphous phase had darker contrast, suggesting lighter elements and/or lower density on average in the intergranular amorphous phase. Furthermore, Ta-rich particles (30–200 nm) were found within

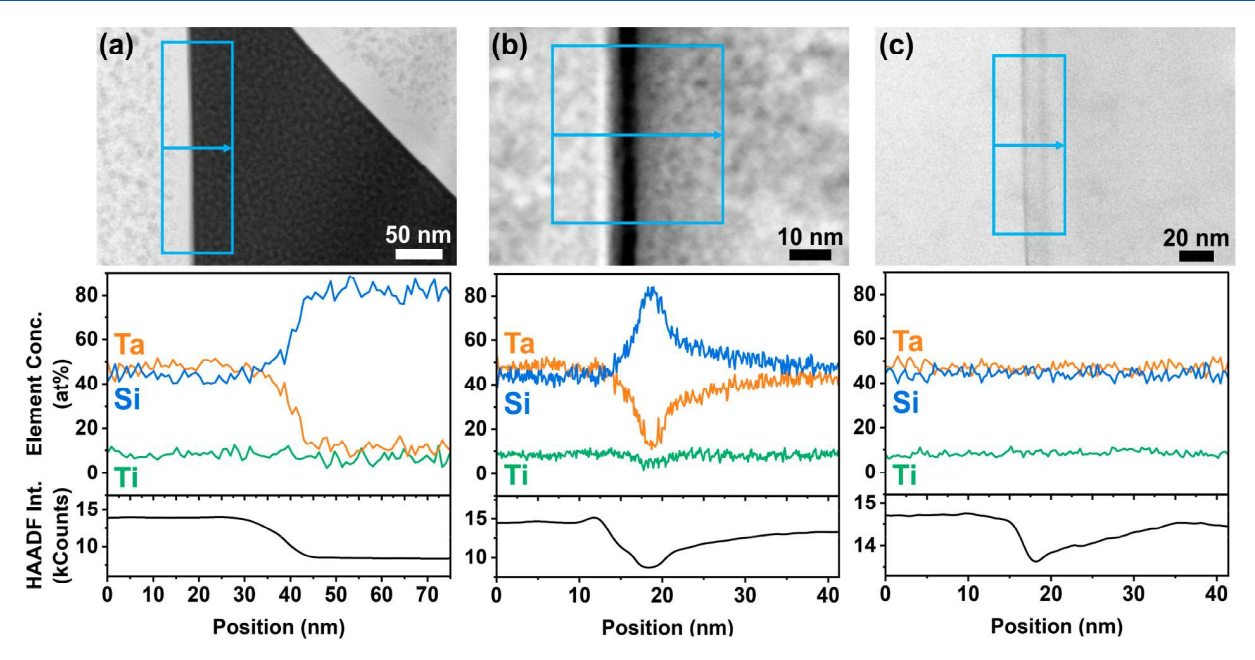


Figure 6. STEM-EDS analysis of different regions in  $\text{Li}_{1.1}\text{Ti}_{0.1}\text{Ta}_{0.9}\text{SiO}_{\text{S}}$  (x=0.1) sintered at 1150 °C for 24 h. The EDS and HAADF intensity signals at each position on the arrow were integrated along the direction perpendicular to the arrow, and the blue box shows the bounds of the region in which the signals were integrated. The elemental distribution and HAADF intensity along the light blue arrow are plotted below each micrograph. The crystalline grains have brighter contrast; the intergranular amorphous phase has darker contrast. (a) A pocket of intergranular amorphous phase between grains with significant Si excess. (b) A thin layer of intergranular amorphous phase between two grains with significant Si excess. (c) A "clean" GB showing an unchanging elemental distribution across it compared with (a) and (b).

some crystalline grains of  $Li_{1+x}Ti_xTa_{1-x}SiO_5$  (Figure S2), which were likely the 1-2 wt % LiTaO<sub>3</sub> observed in XRD. The distribution of the amorphous phase can be categorized into two types: (1) large pockets of intergranular phase filling spaces between grains, particularly at triple points (size: 50-2000 nm, e.g., Figures 5a and 6a); (2) thin layers of amorphous phase along grain boundaries (thickness: 2-4 nm, e.g., Figures 5b and 6b). STEM-EDS was utilized to further analyze the composition of the intergranular phase. In the case of lower Ti dopant concentration (x = 0, x = 0.05), the Si concentration in the thin layers (~60 at. % Si) tends to be lower than that in the large pockets (~80-90 at. % Si), as seen in Figures S3 and 5. In the case of higher Ti dopant concentrations (x = 0.1, 0.15), the composition in the large pockets and the thin intergranular layers was similar, around ~80 at. % Si, as shown in Figures 6 and S4. In either case, the Ti distribution appeared relatively spatially uniform across grains and intergranular regions, and the Ti concentration within the grains matched the nominal dopant concentration, within error. Regardless of the dopant concentration, the amorphous phase consistently had higher Si concentration and lower Ta concentration according to EDS. In addition to thin layers of amorphous phase with Si excess, "clean" GBs without Si excess compared to the grains were also observed in all samples (e.g., Figures 5c and 6c); fewer of these "clean" GBs without excess Si were found in samples with higher dopant concentrations. As the Ti dopant concentration increased, Si-rich amorphous phase(s) (also containing relatively small amounts of Ta and Ti) increased in volume in the intergranular pockets, and a higher fraction of Si-rich grain boundaries were observed (see more discussion in Section 4), concurrent with an increase in the size of such pockets (cf. Figure 4b). Taken together, all these results showed that the distribution and chemistry of the amorphous phase were nonuniform, and each grain boundary or intergranular region

as a result may be expected to behave differently from an electrical standpoint. In later sections, we link the complex spatial and chemical distribution of the intergranular phase and grain boundaries (variation in size and stoichiometry) to a distribution of electrical relaxation times in the intermediate-frequency region of impedance spectra. Additionally, as shown in Figure 4b, we observe reasonable agreement between the intergranular pocket size range observed via microscopy and the average GB width determined electrically by the brick layer model.

3.3. Electrical/Electrochemical Properties of  $Li_{1+x}Ti_xTa_{1-x}SiO_5$ . In terms of electrical properties, DC polarization experiments showed that the measured current decayed rapidly with time under constant voltage, confirming that Li<sub>1+x</sub>Ti<sub>x</sub>Ta<sub>1-x</sub>SiO<sub>5</sub> samples were primarily Li<sup>+</sup> conductors with low electronic and oxygen transference numbers (Li+ transference number: 0.97-0.99, also see Figure S5). The AC impedance spectroscopy measurements revealed that the total conductivities  $(\sigma_{\text{m,total}})$  increased as a function of Ti concentration without significant changes in activation energy  $(E_A)$ , as seen in Figure 7. From x = 0 to x = 0.15,  $\sigma_{\text{m,total}}$  increased by  $\sim$ 1500%, from 8.39  $\times$  10<sup>-7</sup> to 1.25  $\times$  10<sup>-5</sup> S/cm, at 30 °C. While the insertion of Li interstitials raised overall conductivity, the effect of doping on Li transport in the crystalline grains remained elusive without analyzing EIS spectra and separating the transport processes taking place in different microstructural regions and frequency ranges. The Nyquist plots and distribution of relaxation times (DRT) spectra are shown in Figure 8. DRT analysis showed that there were three transport processes within the spectra of the x = 0, 0.05, and 0.10 samples: the high-frequency (HF) peak A, D, or G corresponds to the HF arc in the Nyquist plots, representing grain transport within crystalline grains; the two middle-frequency (MF) peaks B and C, E and F, or H and I can be interpreted as transport processes

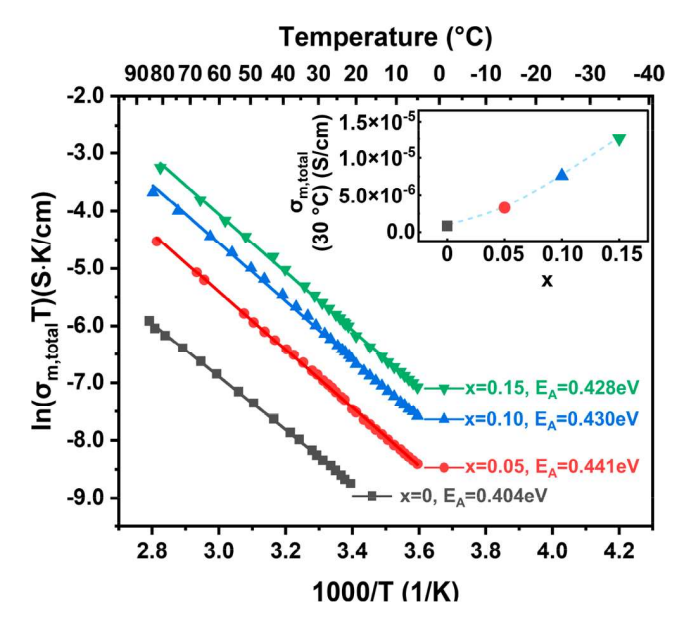


Figure 7. Total conductivities ( $\sigma_{\rm m,total}$ ) of Li<sub>1+x</sub>Ti<sub>x</sub>Ta<sub>1-x</sub>SiO<sub>5</sub> (x=0, 0.05, 0.1, 0.15) as a function of temperature. The inset shows  $\sigma_{\rm m,total}$  at 30 °C for different Ti concentrations. The total conductivity increased as a function of dopant concentration while the total activation energy did not vary significantly. The separation of grain and intergranular phase transport can help elucidate the effect of Li interstitials on the transport processes.

across grain boundaries and the intergranular amorphous phase(s). On the other hand, only two processes can be observed for x = 0.15 in the DRT spectrum, with a HF peak J from grain transport and a broad MF peak K from transport between grains. The HF contributions were attributed to grain transport; the MF contributions were attributed to intergranular transport. The assignments were based on four factors. First, it is well documented that transport within grain boundaries is typically more blocking as compared to the grains in oxide Li<sup>+</sup> conductors, <sup>19,31-34</sup> and as a result (combined with capacitance differences), grain boundary mediated transport is usually assigned to lower-frequency regimes in EIS spectra with higher activation energy than the grains (Figures S8 and S9). Second, the stoichiometry and structure within the grains are observed microscopically to be more homogeneous, giving rise to only one relaxation time, while the variation in the intergranular phase and grain boundaries observed by STEM-EDS can lead to broad distributions of relaxation times in the MF regime (see more discussion in Section 4). Third, the electrical GB widths obtained from these assignments are in reasonable agreement with those observed microscopically (Figure 4b). Fourth, the capacitance of the MF arc is generally higher than that of the HF arc, as expected for interfacial behavior, while the relative permittivity determined from the HF arc capacitance and sample geometry is reasonable for a pure ion conductor in this temperature range (Figure S10).

Despite complicated behaviors in the DRT spectra, the MF transport processes can still be considered as one (depressed) MF arc in the Nyquist plots for equivalent circuit fitting, where the use of a constant phase element (Q in Boukamp notation, where the exponent values of the constant phase elements from the MF arcs ranged between n = 0.68-0.73) captures some of the relaxation time distribution, compared to a perfect capacitor. In fact, it was quite challenging to fit the Nyquist plots with three (RQ) in series and still be confident in the fitting. As a result, an

equivalent circuit of two (RQ) in series, i.e., (RQ)(RQ) in Boukamp notation (any electrode portion was not included in fitting), was used to fit the HF grain transport and MF intergranular transport processes. Grain conductivities  $(\sigma_{ ext{m,grain}})$ increased as a function of dopant concentration from 4.11 ×  $10^{-6}$  (x = 0) S/cm to 2.49 ×  $10^{-5}$  S/cm (x = 0.15) at 30 °C (see Figure 9), while the  $E_A$  decreased from 0.50 to 0.29 eV with increasing Ti content. Plots of  $E_A$  vs dopant concentration are given in Figure S9; the biggest decrease observed was between the undoped x = 0 composition and the slightly doped x = 0.05composition, and  $E_A$  continued to decrease more gradually upon further acceptor doping. The conductivity pre-exponential factor was also observed to decrease in the same way with increasing dopant concentration (Figure S9); the sharpest drop was observed for the initial dopant introduction with more gradual decreases following further Ti and Li content increases. A comparison plot of  $\ln(\sigma_{0,\text{bulk}})$  versus  $E_A$  for the samples with different dopant concentrations can be seen in Figure S8, with the behavior following the Meyer-Neldel rule. While this behavior is consistent with expectations for triggering concerted ion migration within the grains, a discussion of additional experimental methods to further verify concerted ion transport can be found in Section 4.

On the other hand, as the dopant concentration increased and more of the intergranular phase formed, both the effective GB conductivity ( $\sigma_{m,GB,eff}$  Figure S6) and specific GB conductivity ( $\sigma_{m,GB,spec}$ , Figure 10) increased. The  $\sigma_{m,GB,eff}$  is  $5.95 \times 10^{-6}$  S/ cm at 30 °C for x = 0.15. The  $E_A$  values from  $\sigma_{m,GB,eff}$  were higher in doped states compared to the undoped state, which resulted in little change in the total conductivity despite the reduction of  $E_{
m A}$  in grain conductivity. Note that  $\sigma_{
m m,GB,eff}$  represents the ensemble contribution from all the grain boundaries and intergranular regions and is not a local or specific GB conductivity. 35 On the other hand,  $\sigma_{\rm m,GB,spec}$  values, representative of local GB/intergranular transport, were evaluated using electrical grain boundary widths ( $d_{GB}$ ) estimated from the AC-IS data by the brick layer model (eqs 1 and 2), assuming equal grain and grain boundary relative permittivities at all temperatures. The  $E_{\rm A}$  from  $\sigma_{\rm m,GB,spec}$  estimated this way decreased in the same way as the grain conductivity as a function of increasing dopant concentration, with the biggest change upon first introducing the dopant (see Figure S9 and Section 4.2 for more discussion, as the  $E_A$  trend for the specific GB conductivity depends on how it is estimated). Comparing the specific grain boundary conductivity pre-exponential factor and activation energy revealed Meyer-Neldel behavior (Figures S8 and S12). Note that regardless of dopant concentration, GBs remained relatively blocking for Li<sup>+</sup> transport with lower specific conductivities in the GBs relative to the grains. As a result, with the separation of grain and intergranular transport, we can better understand the trends in local transport behavior and conclude that the total conductivity increasing as a function of dopant concentration can be attributed to both grain and GB conductivities increasing. Particularly, isolation of the crystalline lattice response in the grains permits observation of the nonlinear but monotonic trend in decreasing in  $E_A$  with increasing Li interstitial concentration (Figure S9).

As seen in Table 1, LiTaSiO<sub>5</sub> had a calculated wide electrochemical stability window of 1.406–4.106 V vs Li, suggesting excellent stability at high voltages. Cyclic voltammetry (CV) was performed to determine the experimental electrochemical stability window of  $\text{Li}_{1+x}\text{Ti}_x\text{Ta}_{1-x}\text{SiO}_5$ . A slow scan rate of 0.1 mV/s was used to minimize overpotentials and

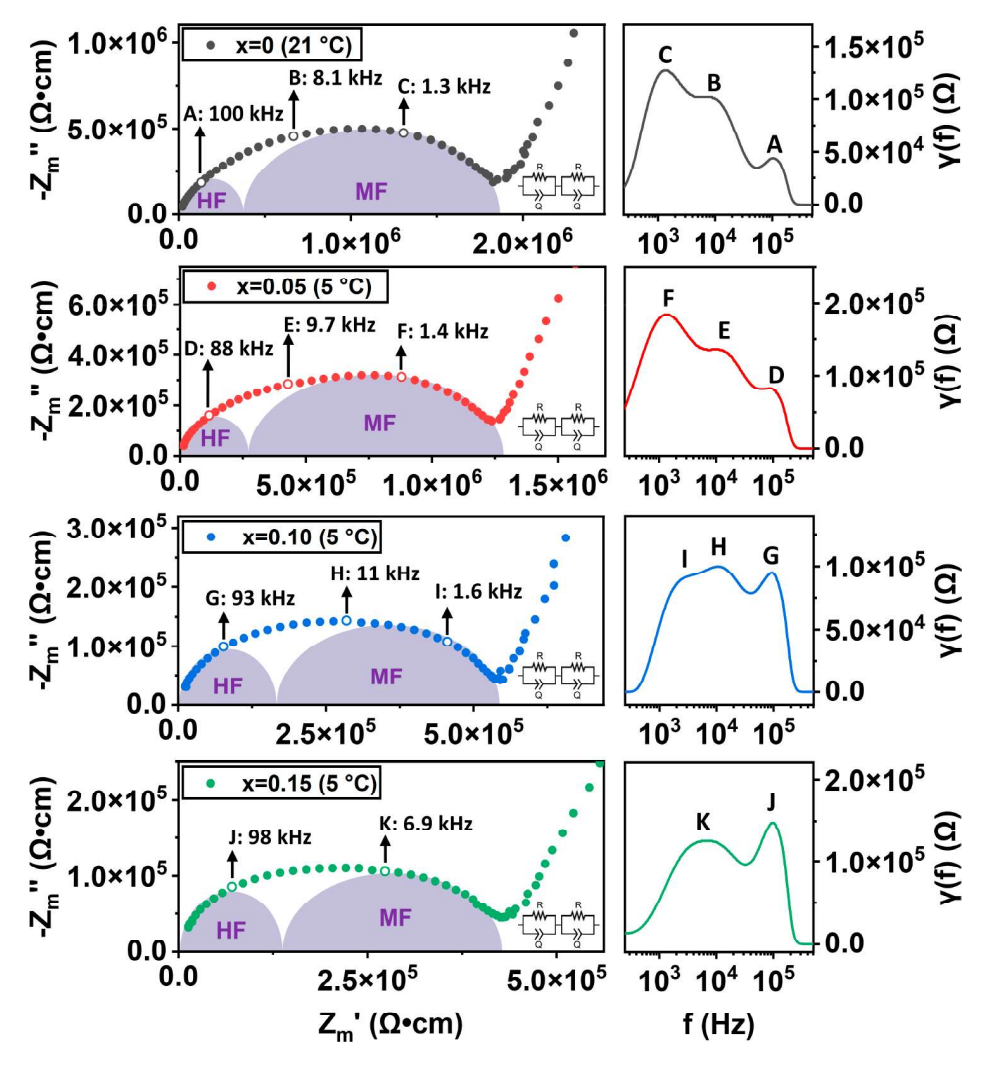


Figure 8. Nyquist plots of  $\text{Li}_{1+x}\text{Ti}_x\text{Ta}_{1-x}\text{SiO}_5$  (x=0,0.05,0.1,0.15). High-frequency (HF) arcs were attributed to grain transport, whereas middle-frequency (MF) arcs were attributed to GB and intergranular amorphous phase transport. The hollow data points on the Nyquist plots mark the peak frequencies from DRT analysis as shown in figures on the right;  $\gamma(f)$  is the distribution function of relaxation times, and f is the relaxation frequency. Nyquist plots of the lowest measurement temperatures for each composition are shown here.  $Z_m$  and  $Z_m$  are respectively the real and imaginary parts of the geometry-corrected impedance. The equivalent circuits used to analyze the spectra are shown in the bottom-right corners of each spectrum. The semicircles serve as approximate eye guides for how the impedance responses were fitted.

more accurately probe the oxidation/reduction limits compared to a fast scan rate. As seen in Figure 11, in the undoped state, an oxidation peak can be seen at 5.03 V, while no significant reduction was observed down to 2 V. With Ti doping, the oxidation potential remained high at ~4.9 V, but the reduction limit increased to  $\sim 2.3$  V. (Note that the higher voltage oxidation peak around  $\sim$ 5.4 V may correspond to  $O_2$  evolution.) In order to test for any reaction between  $Li_{1+x}Ti_xTa_{1-x}SiO_5$  and adjacent Li<sub>6</sub>PS<sub>5</sub>Cl powder during the CV measurements (see Section 2.3), the two electrolyte powders were separately mixed intimately and heat-treated at 200 °C for 2 h. No additional phase was observed in the subsequent XRD pattern (Figure S7), confirming no reaction between Li<sub>1+x</sub>Ti<sub>x</sub>Ta<sub>1-x</sub>SiO<sub>5</sub> and Li<sub>6</sub>PS<sub>5</sub>Cl. In summary, Li<sub>1+x</sub>Ti<sub>x</sub>Ta<sub>1-x</sub>SiO<sub>5</sub> exhibited excellent high voltage stability upon Ti doping, as expected from and exceeding the calculated value; however, the reduction potential increased to some degree.

# 4. DISCUSSION

In this work, it was found that while the grains of  $\operatorname{Li}_{1+x}\operatorname{Ti}_x\operatorname{Ta}_{1-x}\operatorname{SiO}_5$  were mostly crystalline, an amorphous phase was present in intergranular pockets and along some grain boundaries. We first discuss the transport within the crystalline grains, followed by the GB transport, and last the electrochemical stability in terms of processing—structure—property relationships pertinent to electrolyte design.

**4.1. Grain Transport.** By carefully separating HF and MF responses in the EIS measurements, we analyzed grain transport independently. Our results show for the first time a monotonic trend of increasing  $\sigma_{\text{m,grain}}$  and monotonic but nonlinearly decreasing  $E_{\text{A}}$  (into the  $\sim 0.2$  eV range) for Li conduction within the crystalline  $\text{Li}_{1+x}\text{Ti}_x\text{Ta}_{1-x}\text{SiO}_5$  grains as Li was progressively inserted. This observation may provide more direct support for the conclusion of concerted transport drawn from previous studies,  $^{9,10}$  where only total conductivity was investigated, and activation energy varied widely and nonmonotonically with respect to dopant content. As noted (see Figure S9), the reduction of grain conductivity  $E_{\text{A}}$  appears most pronounced

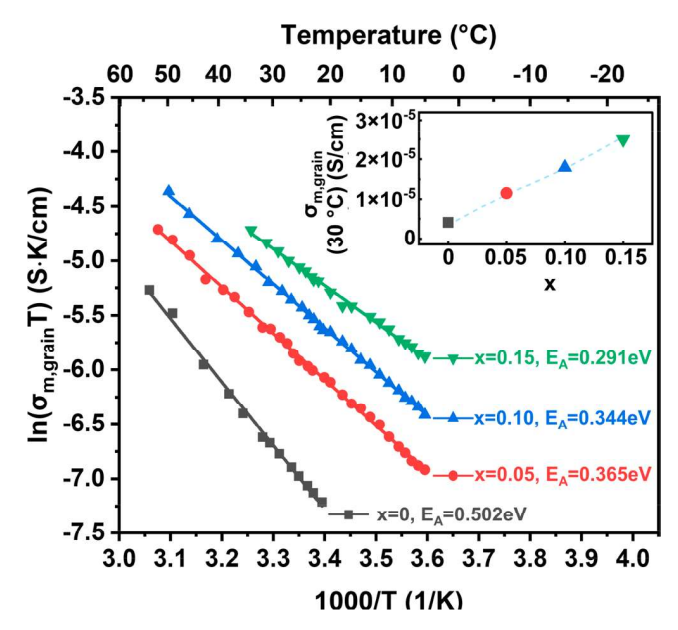


**Figure 9.** Grain conductivities ( $\sigma_{m,grain}$ ) of Li<sub>1+x</sub>Ti<sub>x</sub>Ta<sub>1-x</sub>SiO<sub>5</sub> (x=0, 0.05, 0.1, 0.15) as a function of temperature. The inset shows  $\sigma_{m,grain}$  at 30 °C for different Ti concentrations. The conductivity increased as a function of dopant concentration; activation energy decreased nonlinearly but monotonically as Li interstitials were inserted (see also Figure S9), suggesting concerted ion transport being triggered.

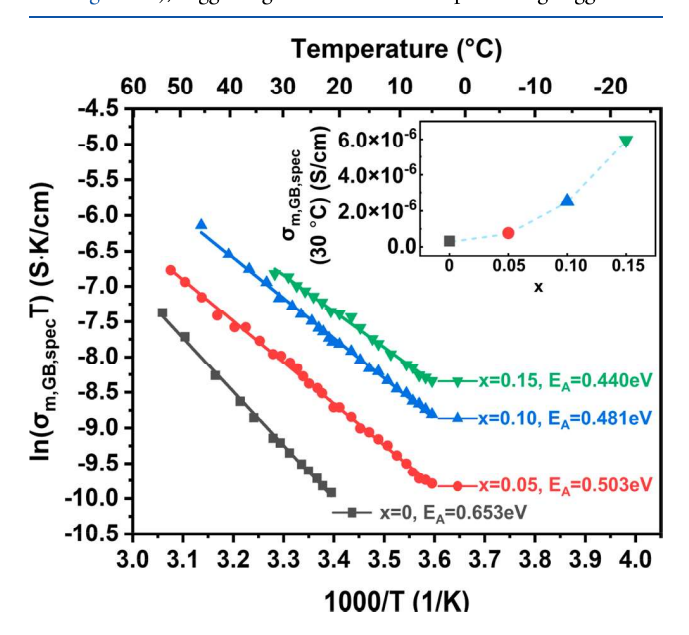
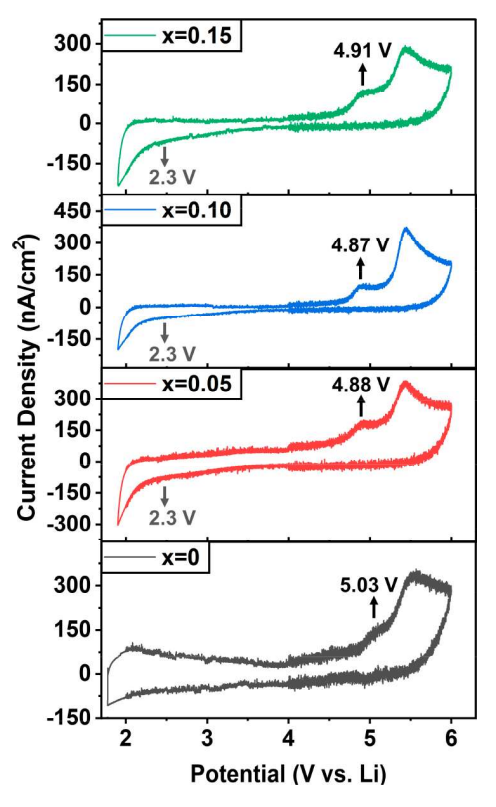


Figure 10. Specific grain boundary conductivities ( $\sigma_{m,GB,spec}$ ) of  $\operatorname{Li}_{1+x}\operatorname{Ti}_x\operatorname{Ta}_{1-x}\operatorname{SiO}_S(x=0,0.05,0.1,0.15)$  as a function of temperature, determined from AC-IS data using the brick layer model with the assumption that grain and grain boundary relative permittivities are equal (eq 1). The inset shows the  $\sigma_{m,GB,spec}$  values at 30 °C for different Ti concentrations. With more Ti dopant and intergranular phase formed, the specific GB conductivity increased while the activation energy decreased nonlinearly but monotonically (see Figure S9) as a function of dopant concentration. However, see Figure S11 for an alternative approach to calculating specific GB conductivity using the microscopically determined average GB widths and grain sizes, which reveals the same trend in the magnitude of conductivity but a different activation energy trend.

going from undoped (x = 0) to x = 0.05, after which point it continues to decrease more gradually with increasing dopant



**Figure 11.** CV of  $\mathrm{Li}_{1+x}\mathrm{Ti}_x\mathrm{Ta}_{1-x}\mathrm{SiO}_5$  (x=0,0.05,0.1,0.15) performed at room temperature at a slow scan rate of 0.1 mV/s to minimize overpotential. High voltage stability can be retained at  $\sim$ 4.9 V upon Ti doping, while the reduction limit increased with a reduction onset of  $\sim$ 2.3 V. Overall,  $\mathrm{Li}_{1+x}\mathrm{Ti}_x\mathrm{Ta}_{1-x}\mathrm{SiO}_5$  exhibited good high-voltage stability.

content (x); insertion of additional Li interstitials in high-energy sites (which may hop downhill under the driving force for ion flux) may increasingly counteract the energy barrier encountered by uphill-climbing ions from low-energy sites. 11,36 In further support of this interpretation, the reduction of  $E_A$ occurred despite the lattice contraction upon doping, which is usually expected to raise  $E_{\rm A}$  and lower conductivity. <sup>19,24,37</sup> We suggest therefore that the reduction of  $E_A$  stemmed primarily from the insertion of Li interstitials instead of from a chemomechanical effect. We may also consider that if the activation energy contains both Li migration and defect generation terms in the undoped (intrinsic) state, the transition to an extrinsic regime upon introduction of the dopant might effectively remove the defect formation energy term. This effect could presumably still coexist with concerted migration in the doped state. Concerted ion transport was also predicted by previous simulation results in  $Li_{1+x}Zr_xTa_{1-x}SiO_5$ , where insertion of Li interstitials led to Li-sublattice disorder and multiple ions hopping in a correlated fashion.  $^{9,10}$  Our experimental grain  $E_A$  of  $0.29 \pm 0.02$  eV corresponds well with the simulated concerted hopping  $E_A$  of 0.25  $\pm$  0.02 eV.<sup>9,10</sup> The observed systematic increase of conductivity and decrease of  $E_A$  with respect to Li concentration and thereby Li site occupancy disordering is suggestive of concerted ion migration, but additional characterization tools may provide further and more direct support for the conduction mechanism as a function of Li content.<sup>19</sup> For example, advanced techniques like pulsed field gradient nuclear magnetic resonance  $(PFG-NMR)^{19,38,39}$  and quasi-inelastic neutron scattering (QENS),<sup>39</sup> each as a function of temperature,

could be of interest to further validate the transport mechanism in future work: By probing tracer and uncorrelated diffusion coefficients using these techniques, we can obtain the Haven ratio to evaluate the number of ions traveling in a correlated fashion.

Studies with even higher dopant concentration (if possible) could be of interest to see if the  $E_A$  continues to decrease or plateaus above x = 0.15 or whether a solubility limit is reached. EDS analysis revealed a ratio of  $Ti/(Ti + Ta) = 0.153 \pm 0.03$ within the grains of the x = 0.15 sample. As a result, it is possible that the solubility limit for Ti had not been reached yet at x =0.15. Therefore, there may be room for a further increase in the dopant concentration and improvements in conductivity. In this case, systematic tuning of synthetic parameters may be needed, as the intergranular phase forms in larger volume fractions at higher dopant concentrations. The increased formation of the intergranular phase at higher Ti concentration may be due to the  $\text{Li}_{1+x}\text{Ti}_x\text{Ta}_{1-x}\text{SiO}_5$  structure becoming less stable: Xiong et al. have shown computationally that the energy above the hull increases with Zr dopant concentration in  $\text{Li}_{1+x}\text{Zr}_x\text{Ta}_{1-x}\text{SiO}_5$ . More discussion regarding the formation of the intergranular phase can be found in Section 5 of the Supporting Information.

The grain conductivity pre-exponential factor decreased in the same way as the activation energy with respect to dopant and Li concentration, consistent with the Meyer—Neldel rule (Figure S8). While doping is expected to generate additional Li interstitial charge carriers that could raise the pre-exponential factor, other dynamic effects that also impact the pre-exponential factor, such as decreased jump distances, attempt frequency, and particularly migration entropy, could be overriding this carrier concentration term.

4.2. Grain Boundary Transport. Next, we consider the impact of the GBs and the intergranular phase on the observed electrical behavior. With such a wide distribution in thickness of the intergranular phase and grain boundaries, the estimations of electrical "grain boundary" widths in the range of 600-900 nm, obtained from the brick layer model analysis of impedance data, were in reasonable agreement with the microscopically observed range of widths of the intergranular phase (see Figure 4b). The estimated electrical grain boundary width also increased with dopant concentration, consistent with the microstructure analysis showing a higher volume fraction of the intergranular phase with increasing Ti content. However, it is important to note that the evaluations of electrical GB widths were only estimates because the brick layer model analysis assumes that the relative permittivities of the grains and the GBs/ intergranular phase are equal at all temperatures. Also, the brick layer model does not account for inhomogeneous GBs/ intergranular phases.

Similarly, considering the DRT analysis, the broad distributions of electrical relaxation times (1–2 broad MF peaks) in the MF range are consistent with the microscopic observation of variation in intergranular phase thickness and stoichiometry. Interestingly, only one broad MF peak K was observed in the DRT spectrum for the x = 0.15 sample (Figure 8), which may be explained by somewhat more homogeneous stoichiometry in the intergranular phase as more Si exsolved. There have also been an increasing number of recent reports demonstrating the fact that each grain boundary in an ionic conductor can behave uniquely, even in samples without amorphous regions.  $^{32,40,41}$ 

To evaluate the local transport in the intergranular phase and grain boundaries, we focus our discussion here on specific GB conductivities. As can be observed from Figures 10, S6, and S9,

the dependence of  $E_A$  on Ti or Li content is different for the specific vs effective GB conductivities, when one makes the assumption in estimating the specific GB conductivity that the grain and grain boundary permittivities are equal at all temperatures in eq 1 (as is common practice in applying the brick layer model). According to eqs 1 and 2, this discrepancy in  $E_{\rm A}$  could in principle arise from temperature-dependent grain boundary widths or temperature-dependent ratio of grain-tograin boundary relative permittivity that was not accounted for. The former is unlikely in intergranular-phase-dominated GBs over the temperature range of the impedance measurements, and indeed the electrical GB widths extracted in this way were not found to be significantly temperature dependent for the doped samples, only for x = 0 with the lower intergranular phase content. Alternatively, in Figure 10 and surrounding analysis, the permittivity ratio was assumed to be 1 and constant with respect to temperature, which may not be the case given the different structure and composition of some GBs vs the grains. To circumvent this potential issue, we also estimated specific GB conductivities using eq 2 and the measured average grain sizes and apparent grain boundary widths from SEM, which were held fixed for all temperatures. The resulting conductivities and related parameters are shown in Figures S11 and S12. In this case, the  $E_A$  values match those of the effective GB conductivity shown in Figure S6. However, regardless of the route taken to applying the brick layer model, the specific GB conductivity was found to increase monotonically with increasing dopant and Li

The formation of the intergranular phase was not necessarily detrimental—the MF transport processes of  $Li_{1+x}Ti_xTa_{1-x}SiO_5$ in this work were less blocking than in some oxide Li conductors 19,31-34 in terms of specific GB conductivities. In fact, the increased formation of the amorphous intergranular phase led to higher specific GB conductivities with increasing Ti content. This result suggests that the "clean" GBs may be more blocking than GBs and pockets containing the amorphous phase and that intentionally promoting formation of the intergranular phase (e.g., via doping or processing conditions) may be beneficial for the local intergranular Li<sup>+</sup> transport. There have also been reports showing that the formation of additional phases instead of "clean" grain boundaries leads to additional benefits. 42-44 For instance, Stegmaier et al. 42 proposed that the formation of complexions along grain boundaries could inhibit dendrite formation in  $Li_{1+x}Al_xTi_{2-x}(PO_4)_3$  (LATP) solid electrolytes. More work is needed to investigate if the intergranular phase in  $Li_{1+x}Ti_xTa_{1-x}SiO_5$  could have other desirable properties (e.g., lower electronic transference numbers) in addition to avoiding large grain boundary resistance. Nevertheless, it could be of interest for future work to take advantage of the formation of the intergranular phase with careful microstructural engineering. For instance, the thickness and composition of the intergranular phase could be engineered by different thermal treatments.

**4.3. Electrochemical Stability.**  $\text{Li}_{1+x}\text{Ti}_x\text{Ta}_{1-x}\text{SiO}_5$  in an undoped state (x=0) was experimentally stable against oxidation up to 5.03 V vs Li, higher than the calculated oxidation limit, as expected. The introduction of Ti was expected to not affect the oxidation limit significantly. This oxidative stability was confirmed by the CV measurements—the oxidation limit only decreased slightly with Ti doping to ~4.9 V. On the other hand, Ti is expected to be less stable to reduction: Ti-containing compositions can reportedly reduce at the relatively high voltage of ~1.7 V<sup>45,46</sup> vs Li. In Li<sub>1+x</sub>Ti<sub>x</sub>Ta<sub>1-x</sub>SiO<sub>5</sub>,

the reduction limit also shifted toward higher potential upon Ti doping. Although the CV measurements were cut off just below 2 V in this study, reduction onsets of around 2.3 V were observed for all Ti-doped samples, while no significant reduction was seen for the undoped sample. The DC polarization results (Figure S5) also indicated that electronic and oxide ion conductivities were negligible, with >97% of the conductivity apparently contributed by mobile Li ions. In summary, Ti doping led to higher ionic conductivity while retaining high oxidation limits in Li<sub>1+x</sub>Ti<sub>x</sub>Ta<sub>1-x</sub>SiO<sub>5</sub>, making it a promising candidate as a thin solid electrolyte or a coating material on the cathode side. Future studies can aim toward studying the decomposition products upon oxidation/reduction—if a stable, electronic-insulating, and passivating interphase forms upon oxidation/reduction, the operating voltage window for a full cell can be wider than the electrochemical stability window measured with CV. In addition, no obvious reaction was found from a heat-treated mixture of Li<sub>1+x</sub>Ti<sub>x</sub>Ta<sub>1-x</sub>SiO<sub>5</sub> and Li<sub>6</sub>PS<sub>5</sub>Cl at 200 °C. This result suggested that the interface between Li<sub>1+x</sub>Ti<sub>x</sub>Ta<sub>1-x</sub>SiO<sub>5</sub> and Li<sub>6</sub>PS<sub>5</sub>Cl during room temperature CV was likely stable. Furthermore, dual (bilayer) electrolyte solid-state cells with wide operating windows could be feasible, potentially even for higher-temperature applications.

# 5. CONCLUSION

In this work, we rediscovered LiTaSiO<sub>5</sub> as a potential new solid electrolyte material by downselecting Li-containing compounds from the Materials Project using a descriptor filter to capture desirable properties for solid electrolytes (i.e., low electronic conductivity, suitable conduction channels, and wide electrochemical stability window). To trigger concerted ion transport in LiTaSiO<sub>5</sub>, 9,10 systematically varied concentrations of Li interstitials were inserted via  ${\rm Ti}_{{\rm Ta}}{}'$  acceptors, making the final composition  ${\rm Li}_{1+x}{\rm Ti}_x{\rm Ta}_{1-x}{\rm SiO_5}$  (0  $\leq x \leq$  0.15).  ${\rm Li}_{1+x}{\rm Ti}_x{\rm Ta}_{1-x}{\rm SiO_5}$  consisted of mostly crystalline grains with an amorphous intergranular phase forming between the crystalline grains. As a result, the transport processes were carefully separated using EIS/DRT and correlated to the microstructure.

In terms of the microstructure, SEM and STEM-EDS revealed a Si-rich/Ta-poor intergranular amorphous phase (varying in size and stoichiometry) formed between the crystalline grains. The amorphous phase formed at a higher volume fraction in samples with a higher dopant (Ti) and lower Ta concentration, which could be attributed to increased instability of the structure. Interestingly, the Ti concentration did not vary much between the grains and the intergranular phase. Consequently, the Ti concentration in the grain remained similar to the nominal overall doping level.

By carefully separating the grain and grain boundary conductivities in EIS spectra and with DRT analysis, we showed for the first time a monotonic increase in grain  $\mathrm{Li}^+$  conductivity along with decreasing grain-specific  $E_\mathrm{A}$  as  $\mathrm{Li}$  interstitials were inserted. Corresponding with previous simulation results of correlated hopping, our results were supportive of  $\mathrm{Li}$  insertion leading to concerted ion transport being triggered within the grains. Advanced techniques like PFG-NMR  $^{19,38,39}$  and QENS  $^{39}$  can be used to further verify the transport mechanism in future work.

The middle-frequency (MF) transport process can be attributed to a combination of transport through the intergranular phase and GBs. As the widths and stoichiometries of the intergranular phase and GBs varied, broad distributions of

relaxation times were observed in the DRT spectra in the MF regime. Overall, while GB/intergranular regions remained blocking relative to the crystalline grains, the specific GB conductivities were not as blocking as in some oxide Li<sup>+</sup> conductors. <sup>19,31–34</sup> In fact, increased formation of the intergranular phase at higher dopant concentrations led to higher specific grain boundary conductivity, potentially due to more intergranular phases forming and replacing some grain boundaries as well as the change in local intergranular phase composition. It could be of interest for future work to engineer the formation of the intergranular phase to optimize its thickness, chemistry, and distribution, which could potentially lead to better electrochemical performance.

In terms of electrochemical stability, although the reduction limit increased to some degree upon Ti doping, the oxidation limit of  $\text{Li}_{1+x}\text{Ti}_x\text{Ta}_{1-x}\text{SiO}_5$  did not vary much, exhibiting excellent high oxidation stability of ~4.9–5 V across different Ti dopant concentrations. DC polarization studies also confirmed the high ionic transference numbers in all samples.

In conclusion,  $\operatorname{Li}_{1+x}\operatorname{Ti}_x\operatorname{Ta}_{1-x}\operatorname{SiO}_5$  compositions are promising  $\operatorname{Li}^+$  conductors with little electronic conductivity and low grain conductivity activation energies upon sufficient acceptor doping. There is also the potential for further improvement in conductivity through either higher dopant concentration or microstructural engineering. Given its wide electrochemical stability window,  $\operatorname{Li}_{1+x}\operatorname{Ti}_x\operatorname{Ta}_{1-x}\operatorname{SiO}_5$  could be a good candidate for application as a thin solid electrolyte or cathode coating material.

## ASSOCIATED CONTENT

# Supporting Information

The Supporting Information is available free of charge at https://pubs.acs.org/doi/10.1021/acsaem.3c01647.

Materials properties calculated; phase fractions, densities, grain sizes, and electrical grain boundary widths of  $\text{Li}_{1+x}\text{Ti}_x\text{Ta}_{1-x}\text{SiO}_5$ ; microstructure of  $\text{Li}_{1+x}\text{Ti}_x\text{Ta}_{1-x}\text{SiO}_5$ ; DC polarization of  $\text{Li}_{1+x}\text{Ti}_x\text{Ta}_{1-x}\text{SiO}_5$ ; possible formation mechanisms for the intergranular phase; effective grain boundary conductivity of  $\text{Li}_{1+x}\text{Ti}_x\text{Ta}_{1-x}\text{SiO}_5$ ; no reactions between  $\text{Li}_{1+x}\text{Ti}_x\text{Ta}_{1-x}\text{SiO}_5$  and  $\text{Li}_6\text{PS}_5\text{Cl}$ ; additional conductivity parameters (PDF)

Excel file listing the compositions in each step of the high-throughput screening process, 3\_Ternary\_data.xlsx (XLSX)

Excel file listing the compositions in each step of the high-throughput screening process, 4\_Quarternary\_data.xlsx (XLSX)

# AUTHOR INFORMATION

## **Corresponding Authors**

Jessica A. Krogstad — Department of Materials Science and Engineering, University of Illinois Urbana—Champaign, Urbana, Illinois 61801, United States; Materials Research Laboratory, University of Illinois Urbana—Champaign, Urbana, Illinois 61801, United States; orcid.org/0000-0003-0628-0501; Email: jakrogst@illinois.edu

Nicola H. Perry — Department of Materials Science and Engineering, University of Illinois Urbana—Champaign, Urbana, Illinois 61801, United States; Materials Research Laboratory, University of Illinois Urbana—Champaign, Urbana, Illinois 61801, United States; orcid.org/0000-0002-7207-2113; Email: nhperry@illinois.edu

#### **Authors**

- Yu-Ying Lin Department of Materials Science and Engineering, University of Illinois Urbana—Champaign, Urbana, Illinois 61801, United States; Materials Research Laboratory, University of Illinois Urbana—Champaign, Urbana, Illinois 61801, United States; orcid.org/0000-0002-7707-1873
- Carlos Juarez-Yescas Department of Chemistry and Materials Research Laboratory, University of Illinois Urbana—Champaign, Urbana, Illinois 61801, United States; orcid.org/0000-0003-4509-6547
- Kai-Wei Lan Department of Materials Science and Engineering, University of Illinois Urbana—Champaign, Urbana, Illinois 61801, United States; Materials Research Laboratory, University of Illinois Urbana—Champaign, Urbana, Illinois 61801, United States
- Paul V. Braun Department of Materials Science and Engineering, University of Illinois Urbana—Champaign, Urbana, Illinois 61801, United States; Department of Chemistry and Materials Research Laboratory, University of Illinois Urbana—Champaign, Urbana, Illinois 61801, United States; orcid.org/0000-0003-4079-8160

Complete contact information is available at: https://pubs.acs.org/10.1021/acsaem.3c01647

#### Notes

The authors declare no competing financial interest.

# ACKNOWLEDGMENTS

This material is primarily based upon work supported by the US Army CERL W9132T-21-2-0008. XRD, SEM, TEM, and sputter coating were performed in the Materials Research Laboratory Central Research Facilities, University of Illinois. The authors also acknowledge the use of XRD instrumentation supported by NSF through the University of Illinois Materials Research Science and Engineering Center DMR-1720633. The authors also acknowledge Jr-Wen Lin for using atom probe tomography as a characterization tool.

# REFERENCES

- (1) Zhang, Z.; Shao, Y.; Lotsch, B.; Hu, Y.-S. S.; Li, H.; Janek, J.; Nazar, L. F.; Nan, C.-W. W.; Maier, J.; Armand, M.; Chen, L. New Horizons for Inorganic Solid State Ion Conductors. *Energy Environ. Sci.* **2018**, *11* (8), 1945–1976.
- (2) Pervez, S. A.; Cambaz, M. A.; Thangadurai, V.; Fichtner, M. Interface in Solid-State Lithium Battery: Challenges, Progress, and Outlook. ACS Appl. Mater. Interfaces 2019, 11 (25), 22029–22050.
- (3) Xiao, Y.; Jun, K.; Wang, Y.; Miara, L. J.; Tu, Q.; Ceder, G. Lithium Oxide Superionic Conductors Inspired by Garnet and NASICON Structures. *Adv. Energy Mater.* **2021**, *11* (37), 2101437.
- (4) Inoue, Y.; Suzuki, K.; Matsui, N.; Hirayama, M.; Kanno, R. Synthesis and Structure of Novel Lithium-Ion Conductor Li7Ge3PS12. *J. Solid State Chem.* **2017**, 246, 334—340.
- (5) Hong, H. Y.-P. Crystal Structure and Ionic Conductivity of Li14Zn(GeO4)4 and Other New Li+ Superionic Conductors. *Mater. Res. Bull.* **1978**, *13* (2), 117–124.
- (6) Thangadurai, V.; Weppner, W. Li6ALa2Nb2O12 (A = Ca, Sr, Ba): A New Class of Fast Lithium Ion Conductors with Garnet-Like Structure. *J. Am. Ceram. Soc.* **2005**, 88 (2), 411–418.
- (7) Xiao, Y.; Jun, K.; Wang, Y.; Miara, L. J.; Tu, Q.; Ceder, G. Lithium Oxide Superionic Conductors Inspired by Garnet and NASICON Structures. *Adv. Energy Mater.* **2021**, *11* (37), 2101437.
- (8) Lin, Y.-Y.; Gustafson, W. J.; Murray, S. E.; Shoemaker, D. P.; Ertekin, E.; Krogstad, J. A.; Perry, N. H. Perovskite Na-Ion Conductors Developed from Analogous Li3xLa2/3-xTiO3 (LLTO): Chemo-

- Mechanical and Defect Engineering. J. Mater. Chem. A Mater. 2021, 9 (37), 21241–21258.
- (9) Xiong, S.; He, X.; Han, A.; Liu, Z.; Ren, Z.; McElhenny, B.; Nolan, A. M.; Chen, S.; Mo, Y.; Chen, H. Computation-Guided Design of LiTaSiO5, a New Lithium Ionic Conductor with Sphene Structure. *Adv. Energy Mater.* **2019**, DOI: 10.1002/aenm.201803821.
- (10) Wang, Q.; Wu, J.-F.; Lu, Z.; Ciucci, F.; Pang, W. K.; Guo, X. A New Lithium-Ion Conductor LiTaSiO5: Theoretical Prediction, Materials Synthesis, and Ionic Conductivity. *Adv. Funct. Mater.* **2019**, 29 (37), 1904232.
- (11) He, X.; Zhu, Y.; Mo, Y. Origin of Fast Ion Diffusion in Super-Ionic Conductors. *Nat. Commun.* **2017**, *8* (1), 15893.
- (12) Catti, M. Short-Range Order and Li+ Ion Diffusion Mechanisms in LiSLa9 2(TiO3)16 (LLTO). Solid State Ion 2011, 183 (1), 1–6.
- (13) Kežionis, A.; Kazakevičius, E.; Kazlauskas, S.; Žalga, A. Metal-like Temperature Dependent Conductivity in Fast Li<sup>†</sup> Ionic Conductor Lithium Lanthanum Titanate. *Solid State Ion* **2019**, 342, 115060.
- (14) Deng, Y.; Eames, C.; Chotard, J.-N.; Lalère, F.; Seznec, V.; Emge, S.; Pecher, O.; Grey, C. P.; Masquelier, C.; Islam, M. S. Structural and Mechanistic Insights into Fast Lithium-Ion Conduction in Li4SiO4-Li3PO4 Solid Electrolytes. *J. Am. Chem. Soc.* **2015**, *137* (28), 9136—9145
- (15) Du, Y. A.; Holzwarth, N. A. W. Li Ion Diffusion Mechanisms in the Crystalline Electrolyte  $\gamma$ -Li<sub>3</sub>PO<sub>4</sub>. *J. Electrochem. Soc.* **2007**, *154* (11), A999
- (16) Lu, X.; Wang, S.; Xiao, R.; Shi, S.; Li, H.; Chen, L. First-Principles Insight into the Structural Fundamental of Super Ionic Conducting in NASICON  $MTi_2(PO_4)_3$  (M = Li, Na) Materials for Rechargeable Batteries. *Nano Energy* **2017**, *41* (July), 626–633.
- (17) Zhang, Z.; Zou, Z.; Kaup, K.; Xiao, R.; Shi, S.; Avdeev, M.; Hu, Y. S.; Wang, D.; He, B.; Li, H.; Huang, X.; Nazar, L. F.; Chen, L. Correlated Migration Invokes Higher Na<sup>+</sup>-Ion Conductivity in NaSICON-Type Solid Electrolytes. *Adv. Energy Mater.* **2019**, 9 (42), 1–14.
- (18) Zhang, B.; Lin, Z.; Dong, H.; Wang, L.-W.; Pan, F. Revealing Cooperative Li-Ion Migration in  $\mathrm{Li}_{1+x}\mathrm{Al}_{x}\mathrm{Ti}_{2-x}$  (PO<sub>4</sub>)<sub>3</sub> Solid State Electrolytes with High Al Doping. *J. Mater. Chem. A Mater.* **2020**, 8 (1), 342–348.
- (19) Lin, Y.-Y.; Yong, A. X. B.; Gustafson, W. J.; Reedy, C. N.; Ertekin, E.; Krogstad, J. A.; Perry, N. H. Toward Design of Cation Transport in Solid-State Battery Electrolytes: Structure-Dynamics Relationships. *Curr. Opin Solid State Mater. Sci.* **2020**, 24 (6), 100875.
- (20) Jain, A.; Ong, S. P.; Hautier, G.; Chen, W.; Richards, W. D.; Dacek, S.; Cholia, S.; Gunter, D.; Skinner, D.; Ceder, G.; Persson, K. A. Commentary: The Materials Project: A Materials Genome Approach to Accelerating Materials Innovation. *APL Mater.* **2013**, *1* (1), 011002.
- (21) Adams, S.; Rao, R. P. Transport Pathways for Mobile Ions in Disordered Solids from the Analysis of Energy-Scaled Bond-Valence Mismatch Landscapes. *Phys. Chem. Chem. Phys.* **2009**, *11* (17), 3210.
- (22) Adams, S. Bond Valence Analysis of Structure-Property Relationships in Solid Electrolytes. *J. Power Sources* **2006**, *159* (1), 200–204.
- (23) Xiao, R.; Li, H.; Chen, L. High-Throughput Design and Optimization of Fast Lithium Ion Conductors by the Combination of Bond-Valence Method and Density Functional Theory. *Sci. Rep* **2015**, *S* (1), 1–11.
- (24) Katcho, N. A.; Carrete, J.; Reynaud, M.; Rousse, G.; Casas-Cabanas, M.; Mingo, N.; Rodríguez-Carvajal, J.; Carrasco, J. An Investigation of the Structural Properties of Li and Na Fast Ion Conductors Using High-Throughput Bond-Valence Calculations and Machine Learning. *J. Appl. Crystallogr.* **2019**, 52 (1), 148–157.
- (25) Rodríguez-Carvajal, J. Recent Advances in Magnetic Structure Determination by Neutron Powder Diffraction. *Physica B Condens Matter* **1993**, *192* (1–2), 55–69.
- (26) Lin, Y.-Y.; Qu, J.; Gustafson, W. J.; Kung, P.-C.; Shah, N.; Shrivastav, S.; Ertekin, E.; Krogstad, J. A.; Perry, N. H. Coordination Flexibility as a High-Throughput Descriptor for Identifying Solid Electrolytes with Li+ Sublattice Disorder: A Computational and Experimental Study. *J. Power Sources* **2023**, *553*, 232251.

- (27) Stevanović, V.; Lany, S.; Zhang, X.; Zunger, A. Correcting Density Functional Theory for Accurate Predictions of Compound Enthalpies of Formation: Fitted Elemental-Phase Reference Energies. *Phys. Rev. B* **2012**, *85* (11), 115104.
- (28) Ruschhaupt, P.; Pohlmann, S.; Varzi, A.; Passerini, S. Determining Realistic Electrochemical Stability Windows of Electrolytes for Electrical Double-Layer Capacitors. *Batter Supercaps* **2020**, *3* (8), 698–707.
- (29) Gates-Rector, S.; Blanton, T. The Powder Diffraction File: A Quality Materials Characterization Database. *Powder Diffr* **2019**, 34 (4), 352–360.
- (30) Wan, T. H.; Saccoccio, M.; Chen, C.; Ciucci, F. Influence of the Discretization Methods on the Distribution of Relaxation Times Deconvolution: Implementing Radial Basis Functions with DRTtools. *Electrochim. Acta* **2015**, *184*, 483–499.
- (31) Wu, J.-F.; Guo, X. Origin of the Low Grain Boundary Conductivity in Lithium Ion Conducting Perovskites: Li3xLa0.67-xTiO3. *Phys. Chem. Chem. Phys.* **2017**, *19* (8), 5880–5887.
- (32) Ma, C.; Chen, K.; Liang, C.; Nan, C.-W.; Ishikawa, R.; More, K.; Chi, M. Atomic-Scale Origin of the Large Grain-Boundary Resistance in Perovskite Li-Ion-Conducting Solid Electrolytes. *Energy Environ. Sci.* **2014**, *7* (5), 1638–1642.
- (33) Dawson, J. A.; Canepa, P.; Clarke, M. J.; Famprikis, T.; Ghosh, D.; Islam, M. S. Toward Understanding the Different Influences of Grain Boundaries on Ion Transport in Sulfide and Oxide Solid Electrolytes. *Chem. Mater.* **2019**, *31* (14), 5296–5304.
- (34) Xu, Q.; Tsai, C.-L.; Song, D.; Basak, S.; Kungl, H.; Tempel, H.; Hausen, F.; Yu, S.; Eichel, R.-A. Insights into the Reactive Sintering and Separated Specific Grain/Grain Boundary Conductivities of Li1.3Al0.3Ti1.7(PO4)3. *J. Power Sources* **2021**, 492, 229631.
- (35) Kidner, N. J.; Perry, N. H.; Mason, T. O.; Garboczi, E. J. The Brick Layer Model Revisited: Introducing the Nano-Grain Composite Model. *J. Am. Ceram. Soc.* **2008**, *91* (6), 1733–1746.
- (36) Morgan, B. J. Lattice-Geometry Effects in Garnet Solid Electrolytes: A Lattice-Gas Monte Carlo Simulation Study. R Soc. Open Sci. 2017, 4 (11), 170824.
- (37) Famprikis, T.; Canepa, P.; Dawson, J. A.; Islam, M. S.; Masquelier, C. Fundamentals of Inorganic Solid-State Electrolytes for Batteries. *Nat. Mater.* **2019**, *18* (12), 1278–1291.
- (38) di Stefano, D.; Miglio, A.; Robeyns, K.; Filinchuk, Y.; Lechartier, M.; Senyshyn, A.; Ishida, H.; Spannenberger, S.; Prutsch, D.; Lunghammer, S.; Rettenwander, D.; Wilkening, M.; Roling, B.; Kato, Y.; Hautier, G. Superionic Diffusion through Frustrated Energy Landscape. *Chem.* **2019**, *5* (9), 2450–2460.
- (39) Gao, Y.; Nolan, A. M.; Du, P.; Wu, Y.; Yang, C.; Chen, Q.; Mo, Y.; Bo, S.-H. Classical and Emerging Characterization Techniques for Investigation of Ion Transport Mechanisms in Crystalline Fast Ionic Conductors. *Chem. Rev.* **2020**, *120* (13), 5954–6008.
- (40) Xu, X.; Liu, Y.; Wang, J.; Isheim, D.; Dravid, V. P.; Phatak, C.; Haile, S. M. Variability and Origins of Grain Boundary Electric Potential Detected by Electron Holography and Atom-Probe Tomography. *Nat. Mater.* **2020**, *19* (8), 887–893.
- (41) Symington, A. R.; Molinari, M.; Dawson, J. A.; Statham, J. M.; Purton, J.; Canepa, P.; Parker, S. C. Elucidating the Nature of Grain Boundary Resistance in Lithium Lanthanum Titanate. *J. Mater. Chem. A Mater.* **2021**, *9* (10), 6487–6498.
- (42) Stegmaier, S.; Schierholz, R.; Povstugar, I.; Barthel, J.; Rittmeyer, S. P.; Yu, S.; Wengert, S.; Rostami, S.; Kungl, H.; Reuter, K.; Eichel, R.-A.; Scheurer, C. Nano-Scale Complexions Facilitate Li Dendrite-Free Operation in LATP Solid-State Electrolyte. *Adv. Energy Mater.* **2021**, *11* (26), 2100707.
- (43) Zheng, C.; Ruan, Y.; Su, J.; Song, Z.; Xiu, T.; Jin, J.; Badding, M. E.; Wen, Z. Grain Boundary Modification in Garnet Electrolyte to Suppress Lithium Dendrite Growth. *Chem. Eng. J.* **2021**, *411*, 128508. (44) Zhu, Y.; Wu, S.; Pan, Y.; Zhang, X.; Yan, Z.; Xiang, Y. Reduced Energy Barrier for Li+ Transport Across Grain Boundaries with Amorphous Domains in LLZO Thin Films. *Nanoscale Res. Lett.* **2020**, *15* (1), 153.

- (45) Zhu, Y.; He, X.; Mo, Y. First Principles Study on Electrochemical and Chemical Stability of Solid Electrolyte-Electrode Interfaces in All-Solid-State Li-Ion Batteries. *J. Mater. Chem. A Mater.* **2016**, *4* (9), 3253–3266.
- (46) Binninger, T.; Marcolongo, A.; Mottet, M.; Weber, V.; Laino, T. Comparison of Computational Methods for the Electrochemical Stability Window of Solid-State Electrolyte Materials. *J. Mater. Chem. A Mater.* **2020**, *8* (3), 1347–1359.